Contents lists available at GrowingScience

Current Chemistry Letters

homepage: www.GrowingScience.com

An MEDT study of Diels-Alder reactions of a tetrahydroazulenone with maleimides: Mechanism, selectivity, and antimicrobial insights

Abdeljabbar Jaddi[a,b], Amine Rafik[a,c], Ouadia Hamlaoui[d], Mohammed Salah[d], Alberto García-Vela[b] and Khadija Marakchi[a*]

[a]*Laboratory of Spectroscopy, Molecular Modelling, Materials, Nanomaterials, Water and Environment, LS3MN2E/CERNE2D, Faculty of Sciences, Mohammed V University in Rabat, Rabat, Morocco*
[b]*Instituto de Física Fundamental, Consejo Superior de Investigaciones Científicas, Serrano 123, 28006 Madrid, Spain*
[c]*Departamento de Ciencias Integradas, Centro de Estudios Avanzados en Física, Matemática y Computación; Unidad Asociada GIFMAN, CSIC-UHU, Universidad de Huelva, Huelva, 21071, Spain*
[d]*Molecular Modelling and Spectroscopy Research Team, Faculty of Science, Chouaïb Doukkali University, P.O. Box 20, 24000, El Jadida, Morocco*

C H R O N I C L E

Article history:
Received January 10, 2025
Received in revised form
March 2, 2025
Accepted April 26, 2025
Available online
April 26, 2025

Keywords:
Diels-Alder cycloaddition reaction
3-methyl-5,6,7,8-tetrahydroazulen-1(4H)-one
7-Norbornenone
MEDT
Molecular docking

A B S T R A C T

The Diels-Alder cycloaddition of cyclopentadienone derivative 3-methyl-5,6,7,8-tetrahydroazulen-1(4H)-one with a series of maleimide derivatives is studied using Molecular Electron Density Theory at the B3LYP/6-311++G(d,p) computational level. Conceptual Density Functional Theory analysis predicts low reaction polarity, which is confirmed by global electron density transfer analysis at the transition structures. Topological analysis reveals the electron distribution and evolution of multiple covalent and non-covalent interactions at the transition structures. The results indicate that these Diels-Alder reactions follow an asynchronous one-step mechanism under kinetic control, favouring the *endo* product formation. Bonding Evolution Theory shows that the reaction mechanism can further be decomposed into five distinct bonding evolution phases. In addition, a molecular docking study is conducted to assess the antimicrobial potential of the reaction products against Escherichia coli and Staphylococcus aureus. An evaluation of the results of binding affinity and molecular interactions concludes that the products are viable as antimicrobial agents.

1. Introduction

The Diels-Alder (DA) cycloaddition reaction is viewed as one of the most useful transformations in organic chemistry.[1,2] The reaction includes the addition of a conjugated diene to a dienophile, resulting in the formation of a six-membered cyclic compound. The DA reaction has played a pivotal role in advancing synthetic strategies for organic compounds with medicinal applications.[3,4] This reaction is also foundational in the industrial production of polymers and agrochemicals, as well as in biological processes like the biosynthesis of natural products and the atmospheric degradation of contaminants.[5,6] Cyclopentadienone derivatives are highly reactive intermediates that have broad utility in organic synthesis required to access complex structures.[7,8] The DA reaction represents a pivotal transformation for constructing norbornenone derivatives.[9] These reactions involve the cycloaddition of electron-deficient olefins with dienes, producing bicyclic norbornenone frameworks. These derivatives are characterized by their remarkable structural stability and distinctive architecture, which render them promising candidates for applications in medicinal chemistry and as intermediates in advanced synthetic pathways. A wealth of experimental and computational studies has been dedicated to exploring the properties, reactivity, and potential applications of norbornenone derivatives, highlighting their importance in both fundamental research and applied chemistry. In 2017, Kueh et al. highlighted their role in drug discovery in a study about norborn-2-en-7-ones as products that release carbon monoxide in response to physiological triggers.[10] Also, Payne et al.

* Corresponding author
E-mail address k.marakchi@um5r.ac.ma (K. Marakchi)

doi: 10.5267/j.ccl.2025.4.002

have used 5-bromo-norborn-2-en-7-one derivatives as a carbon monoxide source for palladium-catalyzed carbonylation reactions[11] emphasizing the chemical versatility of norbornene derivatives in catalysis and drug synthesis. Among norbornenone derivatives, a specific subset of molecules featuring densely substituted 7-norbornenone structures has attracted considerable attention due to its unique properties and significant potential applications.[12,13] The synthesis of the 7-norbornenone scaffold through DA reactions has been extensively studied,[14,15] and the functionalization of 7-norbornenones has been previously shown to be a challenging task with many limitations in the proposed synthetic strategies.[16] Herein, we aim to elucidate the DA reactions of the cyclopentadienone derivative 3-methyl-5,6,7,8-tetrahydroazulen-1(4H)-one (**1a**) as the diene and maleimide (**1b**), N-methylmaleimide (**2b**), N-phenylmaleimide (**3b**), N-tert-butylmaleimide (**4b**), N-methoxymaleimide (**5b**), and N-(*p*) Chlorophenylmaleimide (**6b**) as the dienophiles. The experimental findings demonstrated that the reaction is completely stereoselective, with only the *endo* product being formed.[17] The reactions of **1a** with maleimide derivatives **1b**, **2b**, **3b**, **4b**, **5b**, and **6b** theoretically proceed via two potential reaction pathways. The expected products of the DA reactions are detailed in **Scheme 1**, which also features atom numbering for essential atoms. We employ the Molecular Electron Density Theory (MEDT)[18] to perform a full analysis of these reactions. Modern software tools have significantly enhanced the precision of chemical reaction analysis via density functional theory (DFT)[19] computations. MEDT provides a detailed framework for predicting and understanding chemical reactivity through electron density analysis. MEDT studies have been shown to successfully predict and rationalize reactivity,[20,21] regioselectivity,[22] stereoselectivity,[23] chemoselectivity,[24] steric effects,[25] catalysis,[26] and substituent effects,[27] of various types of chemical reactions with a particular focus on cycloaddition reactions.

The increase in the number of antibiotic-resistant microorganisms coupled with the drive to cut healthcare spending has seen many researchers trying to create additional low-cost antimicrobial agents that do not lead to resistance. Antibiotic drug design is evolving to address the growing challenge of antimicrobial resistance. The key aspects of antibiotic drug design involve identifying bacterial targets, designing molecules that can inhibit the bacterial targets, designing drugs that can overcome the development of bacterial resistance mechanisms, and optimizing the pharmacokinetics and pharmacodynamics of the drugs. Researchers are exploring innovative approaches to develop new classes of antibiotics that can overcome resistance mechanisms. Among many possible approaches such as prodrugs and conjugated oligoelectrolytes (COEs), one promising strategy involves computer-aided drug design, which has been used to create structurally unique antibiotic families targeting essential bacterial enzymes. Fully synthetic compounds, are being designed to bind tightly to bacterial ribosomes, effectively shutting down protein production in both gram-positive and gram-negative bacteria. The products from the DA reactions under consideration in this study were tested against Escherichia coli (E. coli) and Staphylococcus aureus (S. aureus) by the means of molecular docking.[28,29] In humans and several other animals, Escherichia coli is an intestinal inhabiting bacterium. For the most part, this bacterium is not troublesome for human beings, but some strains have the potential to be pathogenic owing to the possession of certain genes. Poor hygiene practices like undercooked meals as well as improper handling of coarse dark meat are the main contributors to E. coli infection. On the other hand, S. aureus is a microbe that works opportunistically and parasitically within the human body, leading to numerous health problems such as sepsis, infectious endocarditis, bone and joint infections, skin and soft tissue infections, and pleuropulmonary infections. In the current study, the proteins **1FJ4** and **3K5M** referring to the FabB enzyme and the DNA Polymerase II respectively, are representatives for Escherichia coli, while proteins **1QME** and **3WQT** referring to the PBP-2X enzyme and the FtsA protein, respectively, are representatives for Staphylococcus aureus bacteria. Binding to these four proteins leads to a disruption in essential bacterial functions and therefore an antibiotic effect.

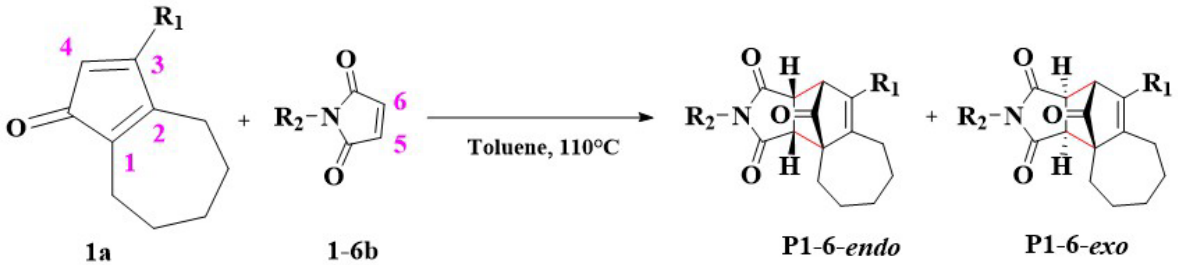

1a 1-6b P1-6-*endo* P1-6-*exo*

1b: R_1=CH_3 **1b: R_2=H**
2b: R_1=H **2b: R_2=CH_3**
3b: R_1=C_6H_5 **3b: R_2=C_6H_5**
4b: R_1=t-Bu **4b: R_2=t-Bu**
5b: R_1=OCH_3 **5b: R_2=OCH_3**
6b: R_1=(*p*)-C_6H_5Cl **6b: R_2=(*p*)-C_6H_5Cl**

Scheme 1. The studied cycloaddition reactions of cyclopentadienone derivatives with various maleimides

2. Computational methods

2.1. Electronic structure calculations

Density functional theory calculations using the B3LYP[30,31] functional and the 6-311++G(d,p) basis set are employed, with optimizations conducted by the Berny analytical gradient method.[32] To characterize the stationary points, frequency calculations were conducted at the same level to ensure that both reactants and products had no imaginary frequencies and that transition structures (TSs) had exactly one imaginary frequency. Intrinsic Reaction Coordinate (IRC)[33] calculations were used to confirm that each TS accurately connected the reactants and products. IRC calculations trace the minimum energy pathway from the TS to the stable configurations of reactants and products, ensuring the correctness of the reaction pathway. All computations were carried out in both the gas phase and within the toluene solvent. For toluene, a self-consistent reaction field (SCRF)[34] using the polarizable continuum model (PCM)[35] was employed to simulate experimental conditions. The calculations were carried out at temperatures 25 and 110 °C. Conceptual Density Functional Theory (CDFT)[36,37] supplies various indices for investigating the reactivity of chemical species. The global electrophilicity index[38] is given by $\omega = \mu^2/2\eta$, where μ is the electronic chemical potential[39] and η is the chemical hardness.[39] This index provides insight into the overall reactivity of the molecules. These parameters can be estimated using frontier molecular orbital energies (E_{HOMO} and E_{LUMO}), with $\mu = (E_{HOMO} + E_{LUMO})/2$ and $\eta = (E_{LUMO} - E_{HOMO})$. The global nucleophilicity index[40] is calculated as $N = E_{HOMO} - E_{HOMO}(TCE)$, with $E_{HOMO}(TCE)$ being -9.49 eV for tetracyanoethylene at the employed level of theory. Tetracyanoethylene (TCE) serves as a reference because of its notably low HOMO energy. The computation of Parr functions[41] involves analysing the Mulliken atomic spin densities of the radical anion and radical cation of the neutral molecule, with $P_k^{-=\rho_s^{rc}(k)}$ and $P_k^{+=\rho_s^{ra}(k)}$. The local nucleophilicity index N_k and local electrophilicity index ω_k are then calculated as $N_k = NP_k^-$ and $\omega_k = \omega P_k^{+\cdot}$ Global electron density transfer (GEDT)[42] is computed by summing the natural atomic charges obtained from Natural Population Analysis (NPA)[43,44] for each framework at the TSs. Positive GEDT values indicate electron density flux from the considered framework to other areas. All calculations were executed using the GAUSSIAN 16 software.[45] The introduction of Quantum Theory of Atoms in Molecules (QTAIM) [46] has revolutionized the way we approach conceptual chemistry, providing a robust method for dissecting electron density within molecules into areas corresponding to individual atoms. This theory offers a clear definition of an "atom in a molecule" and introduces Bond Critical Points (BCPs),[47,48] which are crucial for interpreting the nature and strength of chemical bonds using electron density topology. The Independent Gradient Model Hirshfeld (IGMH)[49] offers a modern visual framework for assessing inter- and intra-fragment interactions. IGMH departs from the original Independent Gradient Model (IGM)[50] method by utilizing atomic densities from the Hirshfeld partition of actual molecular density instead of free-state atomic densities. Within this framework, δg is a key descriptor calculated as $\delta g = |\nabla_\rho^{IGM}| - |\nabla_\rho|$, where $|\nabla_\rho|$ is the electron density gradient, and $|\nabla_\rho^{IGM}|$ is the theoretical upper bound of this gradient, using Hirshfeld-derived atomic densities. Additionally, we utilized the Intrinsic Bond Strength Index for Weak Interactions (IBSIW), available within the Multiwfn package,[51] to quantitatively assess the interaction strengths of bonds forming at the TSs.

The IBSIW is calculated for a given atom pair, i and j, as $IBSIW(i,j) = 100 \times \frac{\delta G_{i,j}^{pair}}{d_{i,j}^2}$,, where $\delta G_{i,j}^{pair}$ represents the specific contribution of the atomic pair to the interaction energy between two fragments. This method offers a precise way to assess and compare bond strengths at TSs, deepening our comprehension of interactions and bond formations in chemical reactions. The IGMH analysis was executed using Multiwfn 3.8, while Electron Localization Function (ELF)[52,53] computations were conducted with the Topmod software.[54] For visualization purposes, we utilized GaussView 6.0[55] and the Visual Molecular Dynamics (VMD) package[56] throughout this study.

2.2. Molecular docking protocol

To explore the binding dynamics and interactions between the selected chemical species and their targets, docking studies were performed using the AutoDock Vina software.[57] The receptor proteins and various ligands were prepared, and grid boxes were set up to cover the active sites using AutoDock 1.5.7 tools available within MGL Tools. The most stable binding conformation of the ligands, identified by the lowest binding affinity, was selected for further analysis of the bonding interactions between ligand atoms and active site residues. The results were visualized using Molecular Operating Environment (MOE),[58] offering in-depth insights into the binding interactions and overall stability.

3. Results and discussion

Analysis of the DA reactions involved in this study is carried out according to the following plan: (i) A CDFT analysis was employed to explore the electronic interactions between the reactants. (ii) Potential energy surfaces along various reaction pathways were explored to assess the energy landscape. (iii)The GEDT at the TSs was used to anticipate polar properties, and the ELF method pinpointed regions of electron density, and a topological analysis, involving QTAIM and IGMH was applied to elucidate the reaction mechanism. Furthermore, Bonding Evolution Theory (BET)[59] was used to analyse the mechanism based on ELF data from IRC points. (iiii) Molecular docking studies were carried out to evaluate the binding interactions and to explore the antimicrobial potential of the DA reaction products against E. coli and S. aureus.

3.1. CDFT indices

CDFT has proven remarkably successful in predicting chemical reactivity and selectivity, particularly in the context of cycloaddition reactions. Its predictive power has been demonstrated across a range of studies.[60-64] CDFT analysis is an integral part of the prediction of electronic properties and reactivity trends for chemical species. The global indices for the interaction of diene **1a** with dienophiles have been calculated at the B3LYP/6-311++G(d,p) level and are presented in **Table 1**, with **Fig. 1** illustrating the progression of the electrophilicity and nucleophilicity indices for the various reactants. The electronic chemical potential of **1a** is μ = -4.36 eV, higher than that of the maleimide derivatives **1b** (μ = -5.55 eV), **2b** (μ = -5.43 eV), **3b** (μ = -5.01 eV), **4b** (μ = -5.24 eV), **5b** (μ = -5.48 eV), and **6b** (μ = -5.07 eV). This indicates an electron density transfer from the diene to the dienophiles. Furthermore, the difference in chemical potential between the diene and the dienophiles reflects the low polarity of these DA reactions. This suggests that these DA reactions can be categorized as Forward Electron Density Flux (FEDF) reactions and this will be explored later when the GEDT is analysed.[65] The nucleophilicity index of the diene **1a** is N = 3.33 eV, which is categorized as a strong nucleophile (N > 2.97 eV), while the dienophiles **1b** (N=1.55 eV), **2b** (N=1.65 eV), **4b** (N=1.97 eV), and **5b** (N=1.72 eV) are weak nucleophiles. On the other hand, the dienophiles **3b** (N=2.55 eV) and **6b** (N=2.60 eV) are moderate nucleophiles.[37,66] However, all reactants exhibit electrophilicity values exceeding 1.90 eV, marking them as strong electrophiles.[37,66] Therefore, the diene **1a** will function as the nucleophile, while the various dienophiles act as electrophiles in these DA reactions. As depicted in **Fig. 1**, all reactants belong to the same zone of electrophilicity which may diminish their reactivity. With respect to the substituents on the position C3 of the diene, all substituted dienes overall show the same electrophilic and nucleophilic behaviour, in the nucleophilicity scale they are all classified as strong nucleophiles while in the electrophilicity scale they are all classified as strong electrophiles indicating that the polarity of the reaction will likely show moderate to low polarity due to the double character of the diene. In any case, the low nucleophilicity of the dienophiles indicate that the diene will behave as a nucleophile.

Table 1. Global CDFT indices in eV of the dienes and the different dienophiles computed at the B3LYP/6-311++G(d,p) level of theory

	E_{HOMO} (eV)	E_{LUMO} (eV)	μ	η	ω	N
1a	-6.16	-2.55	-4.36	3.61	2.63	3.33
2a	-6.32	-2.78	-4.55	3.54	2.93	3.17
3a	-6.16	-2.76	-4.46	3.40	2.92	3.33
4a	-6.14	-2.54	-4.34	3.60	2.62	3.35
5a	-6.03	-2.30	-4.16	3.74	2.32	3.46
6a	-6.28	-2.90	-4.59	3.38	3.12	3.21
1b	-7.94	-3.16	-5.55	4.78	3.22	1.55
2b	-7.84	-3.02	-5.43	4.82	3.06	1.65
3b	-6.94	-3.08	-5.01	3.86	3.25	2.55
4b	-7.59	-2.88	-5.23	4.71	2.91	1.90
5b	-7.77	-3.19	-5.48	4.59	3.27	1.72
6b	-6.89	-3.24	-5.07	3.65	3.51	2.60

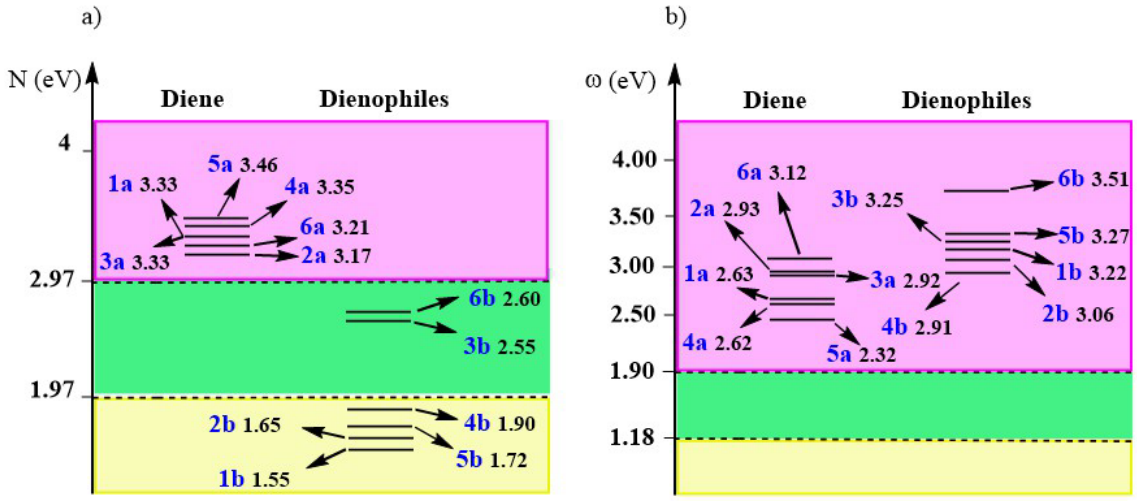

Fig. 1. Nucleophilicity (a) and electrophilicity (b) classification of the dienes and the different dienophiles. Yellow, green, and pink stand for weak, moderate, and strong electrophilicity/nucleophilicity regions, respectively

It is interesting to evaluate other potential reaction pathways between the reactants, notably the potential [2+2] cycloadditions involving the either of the C=C double bonds of the diene with the dienophile or involving the C=O double bonds of either of them. A simple and reliable approach is inspection of the local electrophilicity and nucleophilicity indices. The results are reported for in Supplementary data (**Table 1S**). In the case of maleimides **1-6b**, as reported in literature, the

identity of the N-substituent shows no significant effect on the values of the local electrophilicity index of the molecule and suggests full chemoselectivity towards the C=C double bond. On the other hand, the local electrophilic indices of the diene are more sensitive to the change of the substituent at the C3 position, nevertheless, the diene maintains the highest ωk values at the C1 and C4 atoms. This indicates that the DA reaction considered in **Scheme 1** is indeed the most favourable reaction. Additionally, considering the similar nucleophilic and electrophilic behaviour of all substituted dienes in comparison with the dienophiles as shown by the values of ω and N, in the energetic study we will consider only the reactant 1a as a representative of the series of **1-6a** reactants.

3.2. Energetic details

Due to the symmetry of different maleimides **1b**, **2b**, **3b**, **4d**, **5d**, and **6b**, their DA reactions with diene **1a** are not regioselective. Moreover, these DA reactions offer two stereoisomeric pathways, *endo* and *exo* (**Scheme 1**). In search for stationary points along the *endo* and *exo* reaction paths only a single TS was found connecting the reactants to the products suggesting an asynchronous one-step mechanism in all cases. Therefore, **TS1-*endo***, **TS2-*endo***, **TS3-*endo***, **TS4-*endo***, **TS5-*endo***, and **TS6-*endo*** correspond to the *endo* TSs that yield the *endo* products **P1-*endo***, **P2-*endo***, **P3-*endo***, **P4-*endo***, **P5-*endo***, and **P6-*endo*** while **TS1-*exo***, **TS2-*exo***, **TS3-*exo***, **TS4-*exo***, **TS5-*exo***, and **TS6-*exo***. In contrast, while **TS1-*exo***, **TS2-*exo***, **TS3-*exo***, **TS4-*exo***, **TS5-*exo***, and **TS6-*exo*** represent the *exo* TSs leading to the *exo* products **P1-*exo***, **P2-*exo***, **P3-*exo***, **P4-*exo***, **P5-*exo***, and **P6-*exo*** respectively, as depicted in **Scheme 1**. Values of relative energies, Gibbs free energies, relative enthalpies, and entropies for the stationary points in both the gas phase and toluene solvent at the experimental temperature 110 °C are presented in **Table 2S**, and **Fig. 2** displays a diagram of relative energies, while the geometries of the transition structures for all reaction pathways are depicted in **Fig. 3**. On the other hand, results for calculations at a temperature of 25 °C are shown in **Table 3S**. In the gas phase, evaluation of activation energies showed that **TS1-*endo*** (-428.2 cm^{-1}) is more stable than that **TS1-*exo*** (-434.1 cm^{-1}) by 2.58 $kcal.mol^{-1}$, while **TS2-*endo*** (-418.6 cm^{-1}) is more stable than that **TS2-*exo*** (-433.2 cm^{-1}) by 4.64 $kcal.mol^{-1}$, and lastly, **TS3-*endo*** (-417.3 cm^{-1}) is more favourable than that **TS3-*exo*** (-431.4 cm^{-1}) by 3.08 $kcal.mol^{-1}$. Following the same trend, **TS4-*endo*** (-427.7 cm^{-1}), **TS5-*endo*** (-407.9 cm^{-1}), and **TS6-*endo*** (-414.7 cm^{-1}) are more stable than that **TS4-*exo*** (-432.98 cm^{-1}), **TS5-*exo*** (-419.9 cm^{-1}), and **TS6-*exo*** (-430.8 cm^{-1}) by 2.82, 6.84, and 2.83 $kcal.mol^{-1}$, respectively. The activation barriers are therefore lower for the *endo* approach. On the other hand, with regard to the products, it is the *exo* products that are more stable in all cases, with the *exo* products being 2.87-3.79 $kcal.mol^{-1}$ more stable than the corresponding *endo* products. From a perspective of kinetic control, we observe that the *endo* approach is favourable which aligns with experimental observations and indicates that the reactions were carried out under kinetic conditions. However, the *exo* approach is thermodynamically favoured over the *endo* approach, suggesting that under thermodynamic conditions, the *exo* product would be preferred. The activation enthalpies associated with these DA reactions are 13.32 (**TS1-*endo***), 15.75 (**TS1-*exo***), 12.34 (**TS2-*endo***), 16.91 (**TS2-*exo***), 12.79 (**TS3-*endo***), 15.66 (**T3-*exo***), 14.85 (**TS4-*endo***), 17.60 (**TS4-*exo***), 10.16 (**TS5-*endo***), 16.85 (**TS5-*exo***), 12.54 (**TS6-*endo***) and 15.16 (**T6-*exo***) $kcal.mol^{-1}$. Furthermore, the reaction enthalpies are exothermic between -9.44 and -15.49 $kcal.mol^{-1}$. The effect of toluene as a solvent on the cycloaddition reaction is analysed with a main focus on the activation barriers. In the presence of toluene, the activation energies for **TS1-*endo***, **TS1-*exo***, **TS2-*endo***, **TS2-*exo***, **TS3-*endo***, **TS3-*exo***, **TS4-*endo***, **TS4-*exo***, **TS5-*endo***, **TS5-*exo***, **TS6-*endo***, and **TS6-*exo*** are increased from 12.56, 15.14, 11.68, 16.32, 12.01, 15.09, 14.14, 16.96, 9.44, 16.28, 11.77, and 14.60 $kcal.mol^{-1}$ to 13.28, 15.37, 12.40, 16.80, 13.11, 15.31, 14.78, 17.54, 10.66, 16.43, 12.81, and 14.87 $kcal.mol^{-1}$, respectively. The toluene solvent raised the activation barriers. Furthermore, the activation enthalpies are increased by 0.13-1.16 $kcal.mol^{-1}$ in toluene solvent. Although the solvent did not alter the stereoselectivity, it slightly affects the stability of the products and increases activation energies. Similarly, carrying out the reaction at a lower temperature of 25 °C leads to similar results indicating that the reactions may be carried out experimentally at lower temperatures than 110 °C while maintaining the *endo* selectivity.

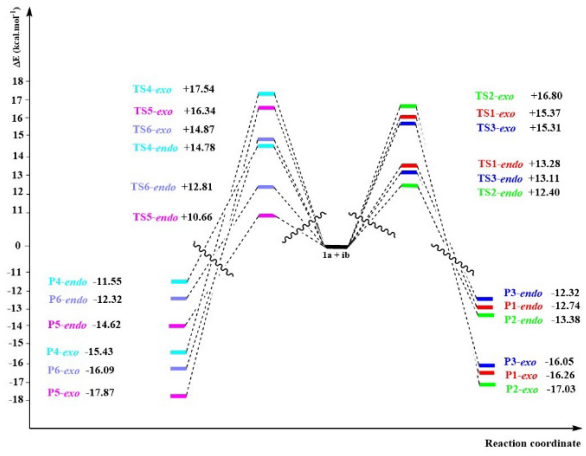

Fig. 2. Reaction energy paths for the DA reactions of cyclopentadienone derivative with different dienophiles in toluene solvent at 110 °C

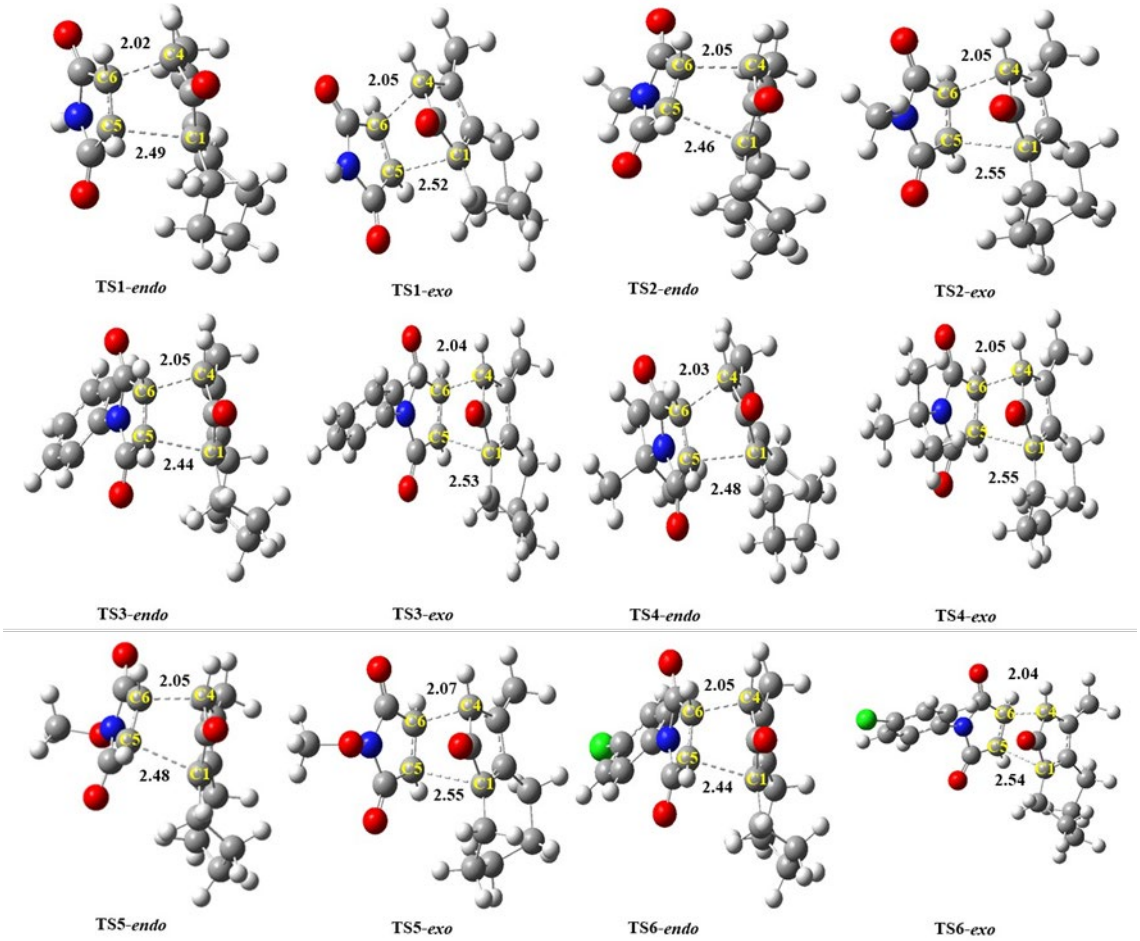

Fig. 3. B3LYP/6-311++G(d,p) optimized geometries of the TSs associated with the DA reactions in toluene solvent . Bond lengths are given in Angtroms.

3.3. Mechanistic study

3.3.1. Analysis of the bond distances at the TSs

The asynchronicity of a reaction is measured by the degree of bond formation, which can be estimated using the l index. This index is calculated as $l = 1 - \frac{r_{x-y}^{TS} - r_{x-y}^{P}}{r_{x-y}^{P}}$, where r_{x-y}^{P} and r_{x-y}^{P} denote the bond distances between atoms x and y in the TS and in the product, respectively.[67] **Table 4S** presents the bond distances of relevant bonds in the TSs and products, along with the l indices for the reaction involving the diene **1a** with the different dienophiles. It is evident that in all pathways, the C4-C6 bond is more advanced than the C1-C5 bond.

3.3.2. Analysis of global electron density transfer

To evaluate the polarity of DA reactions between diene and different dienophiles. we carried out GEDT analyses at the TSs. The GEDT values are presented in **Table 2**. Reactions with GEDT greater than 0.2 e are polar reactions, whereas values under 0.05 e characterize non-polar reactions. For these DA reactions in the gas phase, the GEDT values are 0.15 e for **TS1-*exo***, **TS2-*endo***, **TS2-*exo***, **TS3-*exo***, **TS4-*endo*** and **TS5-*exo***. For **TS1-*endo*** and **TS6-*endo***, the value of GEDT is 0.17 e. **TS3-*endo*** and **TS6-*exo*** have a GEDT value of 0.16 e, while **TS4-*exo*** and **TS5-*endo*** have GEDT values of 0.14 e and 0.18 e, respectively. Although an increase in polarity is observed in toluene, the GEDT values remain below 0.20 e. This suggests that low polarity is a characteristic of these reactions. The values of GEDT are positive; this categorizes these reactions as Forward Electron Density Flux.[65]

Table 2. GEDT for the reactions of diene with various dienophiles in gas phase and in toluene solvent

	Gas phase	Toluene
TS1-*endo*	0.17	0.19
TS1-*exo*	0.15	0.18
TS2-*endo*	0.15	0.16
TS2-*exo*	0.15	0.17
TS3-*endo*	0.16	0.17
TS3-*exo*	0.15	0.18
TS4-*endo*	0.15	0.16
TS4-*exo*	0.14	0.17
TS5-*endo*	0.18	0.19
TS5-*exo*	0.15	0.20
TS6-*endo*	0.17	0.17
TS6-*exo*	0.16	0.19

3.4. Topological analysis

3.4.1. ELF analysis of reactants

Considering the similar reactivity observed for all dienophiles, in the following topological analysis we deem it is sufficient to analyse the wavefunctions of the dienophiles **1-3b** as representatives of the entire series. Topological analysis via the Electron Localization Function method was employed to identify regions of electron localization in the reactants. The findings, such as ELF domains, basin attractor coordinates, and valence basin populations, are depicted in **Fig. 4**. For diene **1a**, the ELF analysis uncovered two disynaptic basins, V(C1,C2) and V'(C1,C2), with a cumulative population of 3.49 e, corresponding to the C1=C2 double bond. Similarly, the C3=C4 double bond showed two disynaptic basins, V(C3,C4) and V'(C3,C4), with a total population of 3.42 e. The C2-C3 single bond was represented by a disynaptic basin, V(C2,C3), with a population of 2.14 e. The ELF analysis of **1b** revealed two disynaptic basins, V(C5,C6) and V'(C5,C6), totaling 3.30 e, associated with the C5=C6 double bond. While the dienophile **2b** similarly displayed two disynaptic basins, V(C5,C6) and V'(C5,C6), with a total population of 3.32 e linked to their C5=C6 bonds. On the other hand, **3b** presented two disynaptic basins, V(C5,C6) and V'(C5,C6), with a total population of 3.31 e connected to their C5=C6 bonds. Atomic charge distributions were assessed using NPA, showing charges on atoms C1, C2, C3, and C4 in diene **1a** of -0.09 e, -0.01 e, +0.06 e, and -0.32 e, respectively, while C5 and C6 atoms in dienophiles **1b**, **2b**, and **3b** carried a charge of -0.22 e.

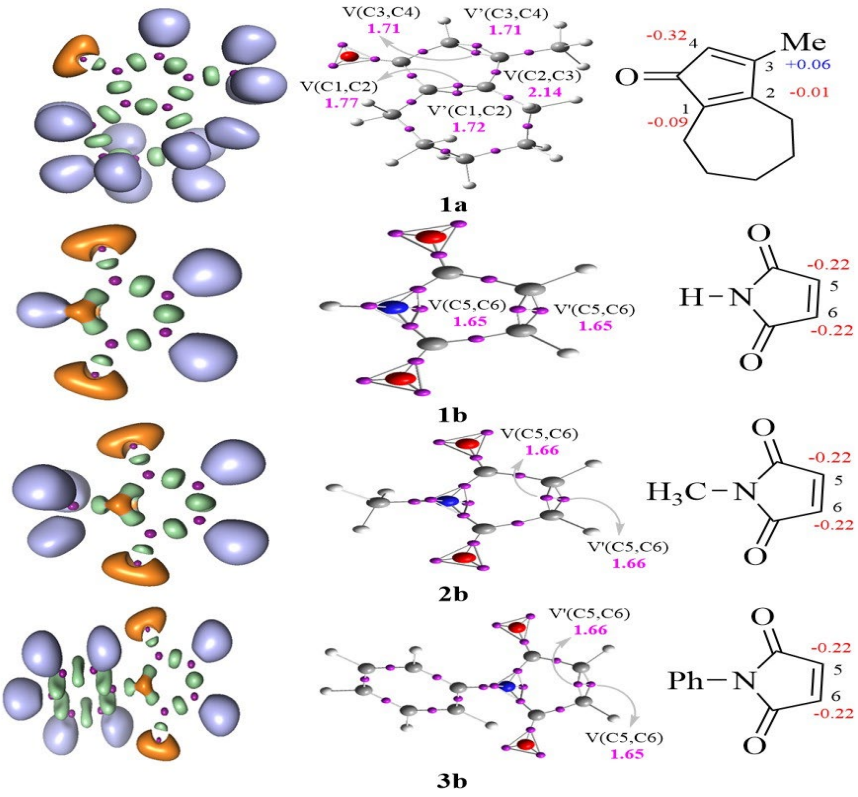

Fig. 4. (Left) ELF localization domains of the reactants plotted at an isosurface value of 0.8. Protonated basins are shown in light purple, monosynaptic basins in orange, disynaptic basins in green, and core basins in purple. (Center) ELF basin attractor positions and population values for the most relevant sites. (Right) Lewis-like structures of reactants and natural atomic charge on reaction sites

3.4.2. ELF analysis of TSs

An ELF analysis was performed to gain a better understanding of the electronic structure of the TSs in the DA reactions. As shown in **Fig. 5**, the ELF localization domains and basin attractor positions were mapped, highlighting the most important valence basin populations. The ELF analysis of the TSs revealed V(C4) monosynaptic basins with electron populations of 0.39/0.35 e in **TS1-*endo*/TS1-*exo***, 0.36/0.35 e in **TS2-*endo*/TS2-*exo***, and 0.36 e in **TS3-*endo*/TS3-*exo***, indicative of a *pseudoradical* center at the C4 carbon atom.[62] The analysis further reveals a V(C6) monosynaptic basin, with electron densities of 0.35 e in **TS1-*endo*** and **TS1-*exo***, 0.33/0.34 e in **TS2-*endo*** and **TS2-*exo***, and 0.34/0.35 e in **TS3-*endo*** and **TS3-*exo***. These findings suggest the presence of a *pseudoradical* center at the C6 position. In diene **1a**, the two disynaptic basins V(C3,C4) and V'(C3,C4), with a combined electron population of 3.42 e, merge into a single V(C3,C4) basin at the TSs. This basin integrates 2.70/2.74 e for **TS1-*endo*/TS1-*exo***, 2.73/2.76 e for **TS2-*endo*/TS2-*exo***, and 2.71/2.75 e for **TS3-*endo*/TS3-*exo***, which associated with the C3-C4 bond region. Similarly, the two disynaptic V(C1,C2) and V'(C1,C2) basins, initially integrating 3.49 e in diene **1a**, combine into a single V(C1,C2) basin in the TSs, with a collective electron population of 3.04/3.06 e for **TS1-*endo*/TS1-*exo***, 3.06/3.09 e for **TS2-*endo*/TS2-*exo***, and 3.06/3.05 e for **TS3-*endo*/TS3-*exo***, corresponding to the C1-C2 bonding region. Additionally, a V(C5) monosynaptic basin is present in the TSs integrating 0.21 e for **TS1-*endo*/TS1-*exo***, 0.18/0.22 e for **TS2-*endo*/TS2-*exo***, and 0.18/0.21 e for **TS3-*endo*/TS3-*exo***, associated with non-bonding electron density at the C5 carbon. The appearance of non-bonding electron density at the C5 carbon and *pseudoradical* centers at C4 and C6, which are not present in the original diene **1a**, occurs as the reaction progresses. The disynaptic basins V(C5,C6) and V'(C5,C6), integrating 3.30/3.33 e in the dienophiles **1b**, **2b**, and **3b**, merge into a single V(C5,C6) basin in the TSs, integrating 2.62/2.65 e across all TSs. The TSs do not show V(C1,C5) and V(C4,C6) disynaptic basins typically linked with new covalent bond formation. However, the C4-C6 bond region has a higher electron density than the C1-C5 bond region, as suggested by the populations of the V(C4) and V(C5) monosynaptic basins. Thus, the DA reactions between diene **1a** and ethylenes **1b**, **2b**, and **3b** occur through a high asynchronous one-step mechanism.

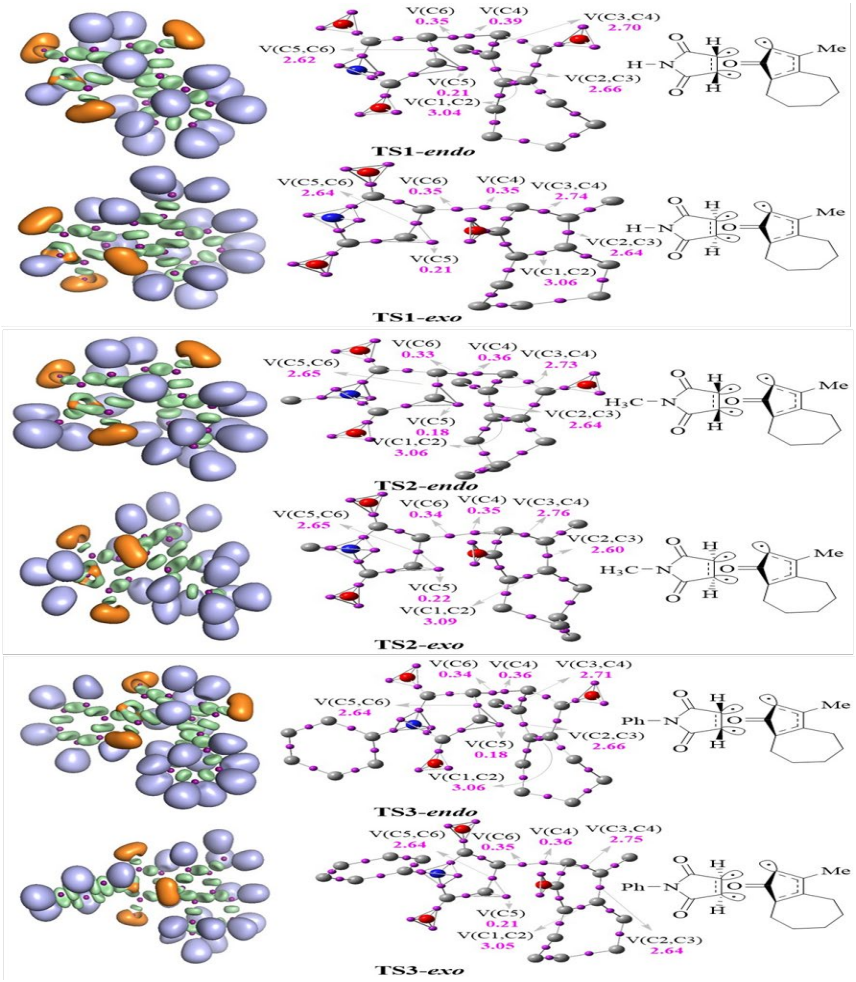

Fig. 5. (Left) ELF localization domains of the TSs of the reaction of diene **1a** with dienophiles **1b**, **2b** and **3b** plotted at an isosurface value of 0.8. Protonated basins are shown in light blue, monosynaptic basins in orange, disynaptic basins in green, and core basins in purple. (Center) ELF basin attractor positions and population values for the important sites. (Right) Lewis-like structures of TSs

3.4.3. Bonding Evolution Theory study of the DA reaction between 1a with maleimide 1b

The BET approach allows for a precise examination of bond evolution throughout a reaction mechanism, providing significant insights into chemical reactivity by tracking the redistribution of electron density along the reaction pathway. To elucidate the mechanism, the ELF topology was analysed at various nuclear configurations along the most energetically favourable path for the DA reaction between **1a** and **1b**, which leads to the formation of **P1-*endo***. The pathway was segmented into five topological phases (I, II, III, IV, and V) through the identification of critical ELF catastrophes. **Table 3** shows the ELF basin populations at selected points on the IRC (**P1**-**P6**), while **Fig. 6** displays the corresponding structures and ELF attractor locations.

At **P1**, the distances d(C1–C5) and d(C4–C6) measure 3.311 Å and 3.121 Å, respectively, and the ELF topology mirrors that of the initial reactants **1a** and **1b**. The two disynaptic basins, V(C1,C2) and V'(C1,C2), with a combined electron population of 3.44 e, represent the C1=C2 double bond. Similarly, two other disynaptic basins, V(C3,C4) and V'(C3,C4), having a total electron population of 3.35 e, correspond to the C3=C4 double bond. Additionally, a disynaptic basin, V(C2,C3), with a population of 2.16 e, is linked to the C2-C3 single bond. The ELF analysis also reveals two disynaptic basins, V(C5,C6) and V'(C5,C6), with a collective population of 3.26 e, corresponding to the C5=C6 double bond.

At **P2**, where d(C1-C5) is 2.642 Å and d(C4-C6) is 2.315 Å, there is a notable shift in the electronic density along the IRC. The two disynaptic basins, V(C1,C2) and V'(C1,C2), which collectively integrate 3.44 e, coalesce into a single V(C1,C2) basin with an integrated 3.24 e, corresponding to the C1-C2 bonding region. Similarly, the V(C3,C4) and V'(C3,C4) basins, which had a combined 3.35 e at **P1**, merge into one V(C3,C4) basin at **P2**, integrating 3.17 e and associated with the C3-C4 bond. Additionally, the V(C5,C6) and V'(C5,C6) basins, initially integrating 3.26 e, merge into a single V(C5,C6) basin at **P2**, integrating 3.14 e, corresponding to the C5-C6 bonding region.

At **P3**, where d(C1-C5) is 2.521 Å and d(C4-C6) is 2.082 Å, three notable changes are observed. This point is marked by the formation of monosynaptic basins V(C4), V(C5), and V(C6) with integrated populations of 0.29, 0.15, and 0.26 e, respectively. The monosynaptic basin V(C4) is linked to the *pseudoradical* center[68] at the C4 carbon, with its electron density arising from the depopulation of the disynaptic basin V(C3,C4), which decreases from 3.17 e at **P2** to 2.82 e at **P3**.

At the **P4**, the bond distances are d(C1-C5) = 2.359 Å and d(C4-C6) = 1.792 Å. The previously observed monosynaptic basins at C4 and C6 have disappeared, and a new disynaptic basin V(C4,C6) appears with a total electron population of 1.30 e. This formation signifies the establishment of a C4-C6 single bond at 1.792 Å due to the coupling of the *pseudoradical* centers at C4 and C6.

Finally, at **P6**, where d(C1-C5) is 1.587 Å and d(C4-C6) is 1.548 Å, a significant change occurs with the formation of the disynaptic basin V(C1,C5), which integrates 1.84 e and is associated with the C1–C5 single bond. The disappearance of the monosynaptic basins at C1 and C5 indicates that the C1–C5 bond has formed through the interaction of the *pseudoradical* centers, now at a distance of 1.587 Å. This leads to a relaxation in molecular geometry and results in the formation of **P1-*endo***.

Table 3. The population valence basin determined from the Electron Localization Function and the newly formed bond distances along the reaction of **1a** with reactant **1b**

Phases	*I*	*II*	*III*	*IV*	*V*	
Points	**P1**	**P2**	**P3**	**P4**	**P5**	**P6**
d(C1,C5)	3.311	2.642	2.521	2.359	2.267	1.587
d(C4,C6)	3.121	2.315	2.082	1.792	1.699	1.548
V(C5,C6)	1.62	3.14	2.74	2.25	2.14	1.88
V'(C5,C6)	1.64	---	---	---	---	---
V(C4)	---	---	0.29	---	---	---
V(C1)	---	---	---	---	0.28	
V(C1,C2)	1.70	3.24	3.09	2.84	2.50	2.05
V'(C1,C2)	1.74	---	---	---	---	---
V(C2,C3)	2.16	2.36	2.58	3.04	3.19	1.79
V'(C2,C3)	---	---	---	---	---	1.75
V(C3,C4)	1.66	3.17	2.82	2.34	2.23	2.02
V'(C3,C4)	1.69	---	---	---	----	----
V(C5)	---	---	0.15	0.46	0.58	---
V(C6)	---	---	0.26	---	---	---
V(C1,C5)	---	---	---	---	---	1.84
V(C4,C6)	---	---	---	1.30	1.48	1.83

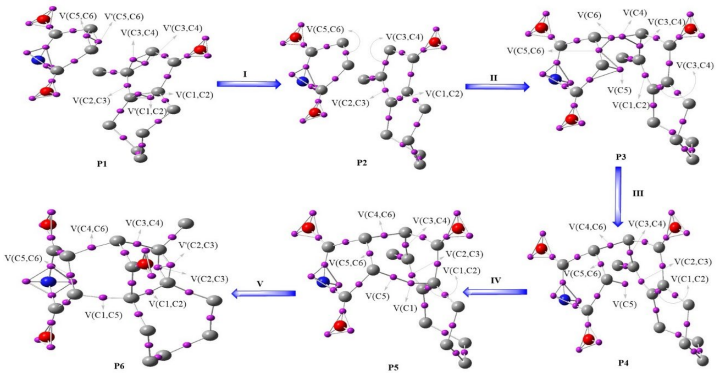

Fig. 6. ELF basin attractor positions of the IRC points **P1**-**P6** of the DA reaction of **1a** with maleimide **1b**

3.4.4. QTAIM analysis of the inter-fragment interactions

QTAIM topological analysis of the electron density ρ at the TSs was performed at the BCPs CP1 and CP2, which are associated with the formation of new C-C single bonds. The QTAIM parameters, listed in **Table 4**, reveal low electron density values and positive Laplacians of the electron density. These findings suggest that non-covalent interactions dominate in the interatomic bonding region, aligning with ELF topological results that indicate no bond formation begins at the TSs.

Table 4. QTAIM parameters (in a.u.) of the (3,-1) BCPs at the TSs corresponding to the DA reactions of diene **1a** with dienophiles **1b**, **2b** and **3b**

	CP1 (C1-C5)		**CP2 (C4-C6)**	
	ρ	**∇2ρ(r)**	**ρ**	**∇2ρ(r)**
TS1-*endo*	0.082	0.016	0.035	0.048
TS1-*exo*	0.078	0.021	0.033	0.048
TS2-*endo*	0.077	0.022	0.038	0.051
TS2-*exo*	0.077	0.022	0.031	0.048
TS3-*endo*	0.077	0.022	0.039	0.051
TS3-*exo*	0.078	0.021	0.032	0.048

3.4.5. IGMH analysis of the inter-fragment interactions

Analysis of IGMH results provides valuable insights into the evolution of electron density at the TS level, evaluates the asynchronicity of the reactions, and investigates the factors contributing to the stability of TSs. The IGMH method can for instance, establish a clear connection between molecular species geometries and their stability.[69,70] The findings related to the reaction between diene **1a** with dienophiles **1b**, **2b**, and **3b** are depicted in **Fig. 7** and **Fig. 8**. It is evident that the interaction regions in **TS1-*endo***, **TS2-*endo***, and **TS3-*endo***, corresponding to an *endo* approach, exhibit significantly larger isosurfaces compared to their *exo* counterparts **TS1-*exo***, **TS2-*exo***, and **TS3-*exo***. The larger isosurface suggests the presence of attractive non-covalent interactions between diene **1a** with dienophiles **1b**, **2b**, and **3b**. These findings shed light on the forces influencing molecular interactions in these reactions and offer an explanation for the *endo* pathway's preference in DA reactions.

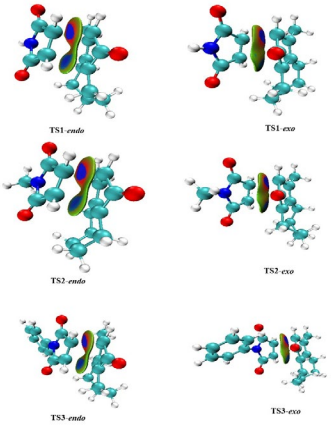

Fig. 7. sign (λ2)ρ colored isosurfaces of δg^{inter} = 0.16 a.u of TSs of reactions of diene **1a** with dienophiles **1b**, **2b**, and **3b**. Green is for Van der Waals forces, blue is for attractive interactions, and red is for repulsive interactions

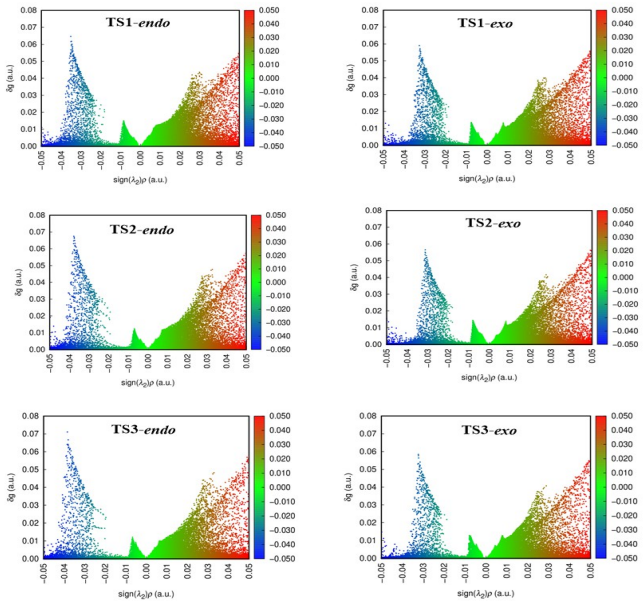

Fig. 8. δg values for the TSs involved in the DA reactions between cyclopentadienone derivative **1a** with maleimide derivatives **1b**, **2b**, and **3b**

The Intrinsic Bond Strength Index for Weak Interactions is used to determine the strength of interactions at all TSs. **Fig. 9** shows that among the IBSIW values of the newly forming σ bonds, the C4-C6 bond progresses more quickly than the C1-C5 bond, indicating an asynchronous bond formation process. This is consistent with the previous findings aggregated by the *l* index.

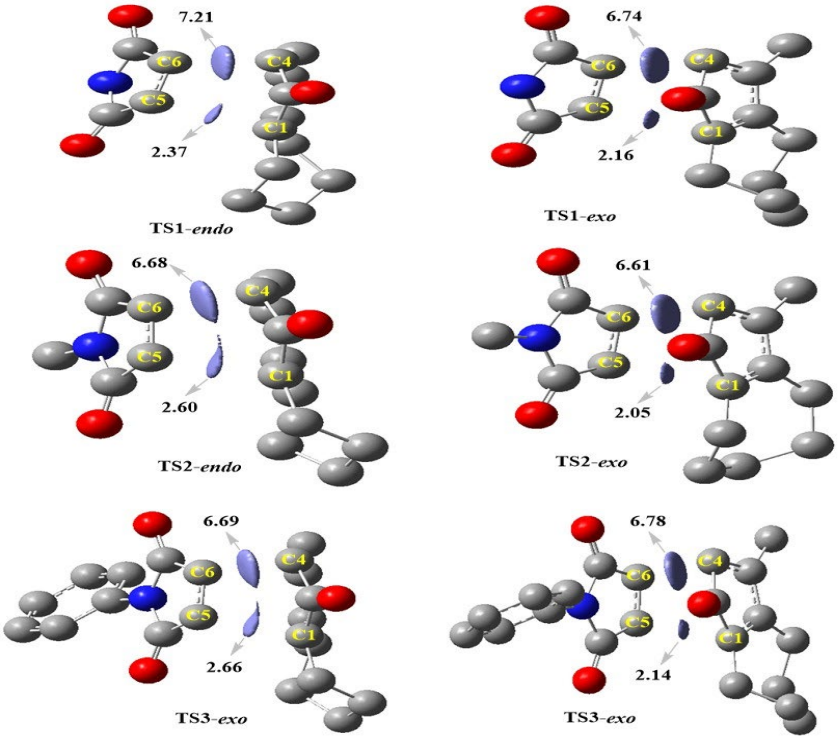

Fig. 9. IBSIWs for TSs of the reaction of diene **1a** with dienophiles **1b**, **2b** and **3b**

3.5. Molecular docking analysis

Molecular docking permits evaluating the interaction of molecules with protein binding sites. In this study, we evaluate the inhibitory potential of the DA reaction products (**P1-*endo***, **P1-*exo***, **P2-*endo*, P2-*exo***, **P3-*endo***, **P3-*exo***, **P4-*endo***, **P4-*exo***, **P5-*endo***, **P5-*exo***, **P6-*endo*** and **P6-*exo***) as antimicrobial agents against E. coli and S. aureus. We determine the binding energies of the protein-ligand interactions and identified potential ligand binding sites within the proteins.

3.5.1. E. coli bacteria

The proteins **1FJ4** and **3K5M** are critical to the survival of E. coli. **1FJ4** is a key enzyme in fatty acid biosynthesis, necessary for membrane formation, while **3K5M** is involved in DNA replication and repair. Inhibiting of either of them leads to a disruption in the function of the cell and potentially to bacterial death. Targeting these proteins with antibiotics weakens bacterial integrity and survival, making them promising drug targets.

The ligands are evaluated based on their binding energies, with lower binding energies indicative of higher binding affinities, larger surface areas, and increased hydrogen bond interactions. The docking results for all ligands with the E. coli target are summarized in **Table 5**. According to the findings, all the ligands show some relevant interactions with the receptor. In particular, the **P6-*endo*** shows the highest affinity for the target receptors, with binding energies of -9.6 kcal.mol^{-1} for **1FJ4**, and -8.3 kcal.mol^{-1} for **3K5M**. As a result, the **P6-*endo*** compound has the highest potential for efficacy against E. coli. The binding mode for E. coli proteins with the **P6-*endo*** using an enzymatic pocket for 2D ligand interaction with specific amino acids and a 3D view for H-bonds, is illustrated in **Fig. 10** and **Fig. 11**.

Table 5. Binding affinities (kcal.mol^{-1}) of E. coli proteins using Autodock Vina

Ligands	Proteins	
	1FJ4	3K5M
P1-*endo*	-6.3	-7.5
P1-*exo*	-6.8	-7.4
P2-*endo*	-6.5	-7.4
P2-*exo*	-6.4	-7.8
P3-*endo*	-7.3	-8.0
P3-*exo*	-8.1	-7.7
P4-*endo*	-8.7	-7.5
P4-*exo*	-7.0	-7.5
P5-*endo*	-8.3	-7.2
P5-*exo*	-6.6	-7.6
P6-*endo*	-9.6	-8.3
P6-*exo*	-8.8	-8.1

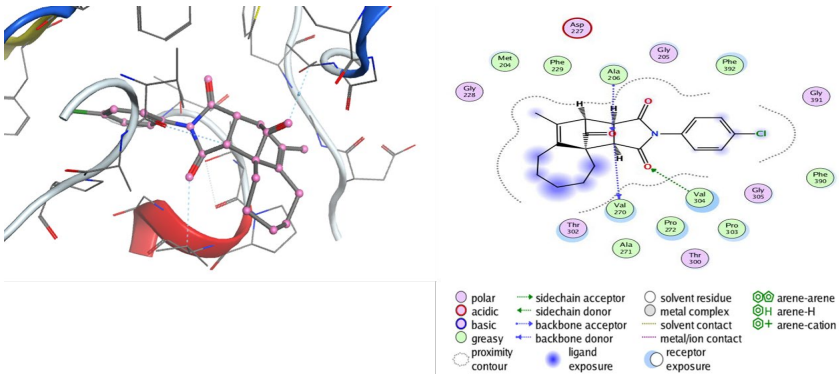

Fig. 10. (Right panel) 2D view of the binding conformation of the **P6-*endo*** inhibitor at the active site of **1FJ4** protein. (Left panel) 3D view for H-bonds

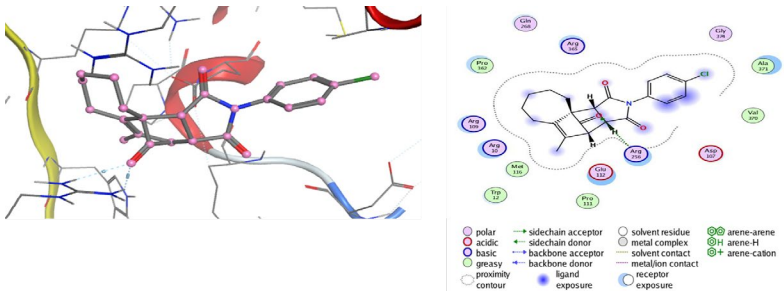

Fig. 11. (Right panel) 2D view of the binding conformation of the **P6-*endo*** inhibitor at the active site of **3K5M** protein. (Left panel) 3D view for H-bonds

Table 6 presents the various interactions between the **P6-*endo*** ligand and the amino acids of the considered protein. It is evident that **P6-*endo*** is the most active compound from the studied series. It interacts with the active site through H-donor with amino acid VAL 270 (3.90 Å), H-acceptor with amino acids VAL 304 (3.24 Å) and ALA 206 (3.50 Å) for **1FJ4**. Moreover, for **3K5M**, **P6-*endo*** has an H-acceptor interaction with amino acids ARG 256 (3.80 Å) and ARG 256 (3.14 Å).

Table 6. Interaction between the **P6-*endo*** ligand and relevant amino acids

Proteins	Active site Amino acids	Interactions Types	Distances (A°)
1FJ4	VAL 270	H-donor	3.90
	VAL 304	H-acceptor	3.24
	ALA 206	H-acceptor	3.50
3K5M	ARG 256	H-acceptor	3.36
	ARG 256	H-acceptor	3.14

3.5.2. S. aureus bacteria

The proteins **1QME** and **3WQT** are two of the most important proteins that can be targeted to induce an antimicrobial effect against the S. aureus bacteria. In particular, binding to **1QME**, inhibits cell wall formation and causes bacterial lysis, while inhibiting **3WQT** disrupts cytokinesis, preventing bacterial replication. **Table 7** presents the docking analysis results for S. aureus bacteria. It revealed that **P1-*exo*** and **P6-*exo*** had the highest affinity for the target receptors. Specifically, **P6-*exo*** demonstrated binding energies of -9.6 kcal.mol^{-1} for **1QME**. In contrast, **P1-*exo*** had the binding energies of -10.8 kcal.mol^{-1} for **3WQT**. These results indicate that **P1-*exo*** and **P6-*exo*** exhibit the most significant potential activity against S. aureus bacteria. Penicillin is one of the most common antibiotics, and it is well known to bind to the **1QME** protein, inhibiting its enzymatic activity. We have made a comparison of the binding energy of our molecules with that of penicillin as a reference. The results indicate that our compounds had comparable or even stronger binding affinities in some cases to the biological target than penicillin which has a binding energy of -7.8 kcal.mol^{-1}.[71] The interaction between S. aureus proteins and the **P1-*exo*** and **P6-*exo*** are illustrated in **Fig. 12** and **Fig. 13**, with the enzymatic pocket depicted for 2D ligand interaction with specific amino acids and a 3D view showing hydrogen bonds.

Table 7. Binding affinities (kcal.mol^{-1}) of S. aureus proteins using Autodock/vina

Ligands	Proteins	
	1QME	**3WQT**
P1-*endo*	-7.8	-8.0
P1-*exo*	-8.0	-10.8
P2-*endo*	-7.8	-7.7
P2-*exo*	-8.3	-9.5
P3-*endo*	-8.2	-8.8
P3-*exo*	-7.7	-9.4
P4-*endo*	-8.2	-8.1
P4-*exo*	-8.0	-8.3
P5-*endo*	-7.7	-7.8
P5-*exo*	-8.5	-7.7
P6-*endo*	-9.0	-8.7
P6-*exo*	-9.6	-8.5
Penicillin	-7.8	---

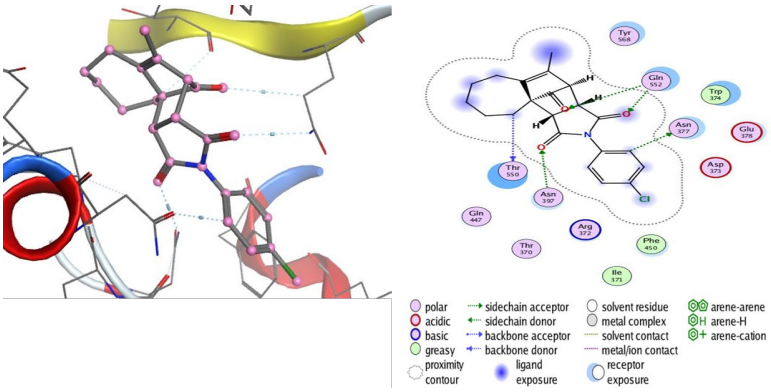

Fig. 12. (Right panel) 2D view of the binding conformation of the **P6-*exo*** inhibitor at the active site of **1QME** protein. (Left panel) 3D view for H-bonds

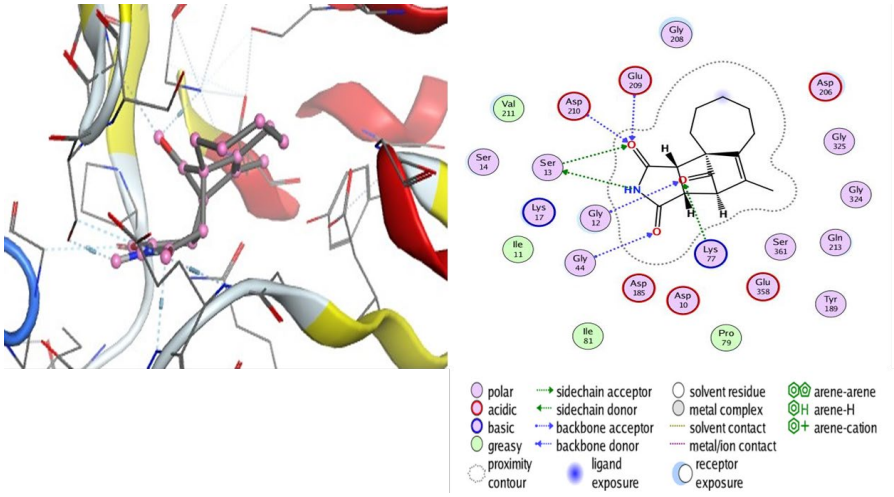

Fig. 13. (Right panel) 2D view of the binding conformation of the **P1-*exo*** inhibitor at the active site of **3WQT** protein. (Left panel) 3D view for H-bonds

The results in **Table 8** indicates the different interactions between the most active ligands **P6-*exo*** and **P1-*exo***. **P6-*exo*** interacts with the active site through an H-donor with amino acids THR 550 (3.19 Å) and ASN 377 (2.97 Å), H-acceptor with amino acids GLN 552 (3.25 Å), GLN 252 (3.00 Å) and ASN 397 (2.80 Å) for **1QME**. On the other hand, the **P1-*exo*** compound interacts with the active site via an H-donor with amino acid SER 13 (3.75 Å), and an H-acceptor with amino acids GLY 12 (3.30 Å), LYS 77 (3.65 Å), GLY 44 (3.48 Å), SER 13 (3.50 Å), GLU 209 (2.90 Å) and ASP 210 (2.97 Å) for **3WQT**.

Table 8. Interaction between the **P6-*exo*** and **P1-*exo*** ligands and relevant amino acids

Proteins	Ligands	Active site Amino acids	Interactions Types	Distances (A°)
1QME	**P6-*exo***	THR 550	H-donor	3.19
		ASN 377	H-donor	2.97
		GLN 552	H-acceptor	3.25
		GLN 552	H-acceptor	3.00
		ASN 397	H-acceptor	2.80
3WQT	**P1-*exo***	SER 13	H-donor	3.75
		GLY 12	H-acceptor	3.30
		LYS 77	H-acceptor	3.65
		GLY 44	H-acceptor	3.48
		SER 13	H-acceptor	3.50
		GLU 209	H-acceptor	2.90
		ASP 210	H-acceptor	2.97

3.6. ADMET

3.6.1. Pharmacokinetic and drug-likeness assessment of the compounds

ADMET has been carried out to evaluate drug-like properties of the compounds considered in this study. **Table 5S** presents the pharmacokinetic and physicochemical properties of the different compounds (**P1-*endo/exo***, **P2-*endo/exo***, **P3-*endo/exo***, **P4-*endo/exo***, **P5-*endo/exo***, and **P6-*endo/exo***). The parameters are categorized into Absorption, Distribution, Metabolism, Excretion, and Lipinski's Rule of 5 to assess drug-likeness. In here, we summarize the results in the table. The results indicate that all compounds exhibit low water solubility, which may impact their dissolution and absorption rates. Despite this, their high intestinal absorption suggests strong potential for oral administration. The Caco-2 permeability values indicate favourable membrane permeability for most compounds, except **P5-*endo/exo***, which shows limited permeability. Skin permeability values suggest poor transdermal absorption for all compounds. Regarding distribution, the volume of distribution (VDss) values indicates moderate to high tissue penetration for **P3-*endo/exo*** and **P6-*endo/exo***, whereas **P1-*endo/exo*** shows the lowest distribution, suggesting it remains primarily in plasma. Blood-brain barrier (BBB) permeability and CNS permeability values suggest that none of the compounds effectively cross the BBB, minimizing the likelihood of central nervous system effects. From a metabolic perspective, all compounds are CYP3A4 substrates, indicating a primary metabolism through this pathway. Additionally, **P3-*endo/exo*** and **P6-*endo/exo*** inhibit CYP2C19, which may lead to drug-drug interactions when co-administered with other medications metabolized by CYP2C19. The absence of inhibitory activity toward CYP1A2, CYP2C9, CYP2D6, and CYP3A4 suggests a lower risk of metabolic interference. In terms of excretion, **P4-*endo/exo*** exhibits the highest clearance, suggesting rapid elimination, while **P1-**

endo/exo and **P5-*endo/exo*** have lower clearance, indicating prolonged systemic retention. Only **P4-*endo/exo*** is an OCT2 substrate, implying that renal excretion is not a significant pathway for most compounds. According to Lipinski's Rule of 5, all compounds meet the criteria for oral drug-likeness, reinforcing their potential as orally bioavailable therapeutic agents. Overall, Both **P1-*endo/exo*** and **P6-*endo/exo*** have promising ADMET properties for oral administration, but **P1-*endo/exo***'s low distribution and **P6-*endo/exo***'s potential drug-drug interactions may pose limitations.

3.6.2. Toxicity risks and drug-likeliness

The analyzed compounds (**Table 6S**), with the exception of **P6-*endo/exo***, have a predicted LD50 of 1000 mg/kg and are classified under Toxicity Class 4, indicating moderate toxicity. In contrast, **P6-*endo/exo*** exhibits a higher LD50 of 7000 mg/kg and is categorized as Toxicity Class 6, suggesting a lower acute toxicity risk. The prediction accuracy for these compounds ranges from 68.07% to 70.97%, reflecting a moderate level of confidence in the toxicity predictions. Additionally, the average similarity values show some variation, with **P1-*endo/exo***, **P2-*endo/exo***, and **P4-*endo/exo*** having the highest similarity (88.79%), while **P6-*endo/exo*** has the lowest (66.83%). This variation may be due to structural or chemical differences that impact the prediction model's assessment of toxicity. Overall, the majority of the compounds share similar toxicity profiles, except for **P6-*endo/exo***, which appears to have a more favourable safety profile.

4. Conclusion

The DA reactions involving the 3-methyl-5,6,7,8-tetrahydroazulen-1(4H)-one with a series of maleimide derivatives were studied through MEDT, utilizing DFT calculations at the B3LYP/6-311++G(d,p) level. CDFT indices predict low polarity for these reactions, with electron density transfer from the nucleophilic diene to the electrophilic maleimide derivatives, which was confirmed by GEDT analyses at the TSs, classified as FEDF. This indicates that the reactions may be favoured by low polarity solvents. These reactions proceed via a high asynchronous one-step mechanism and are kinetically controlled with exclusive *endo* stereoselectivity. The activation energy for the *endo* pathway is lower than that for the *exo*, aligning with experimental results. Additionally, the results indicate that the reaction may be carried out at lower temperature and with more substituents on the N position of the dienophile, all while maintaining the *endo* selectivity. ELF analysis indicates that the formation of new covalent bonds has not yet started at the TSs, while QTAIM analysis reveals the presence of several non-covalent interactions at the TSs. The formation of new C-C single bonds is asynchronous. Bonding Evolution Theory further breaks down the reaction mechanism into five phases, characterized by distinct electronic density distribution patterns, highlighting the changes occurring as the reaction evolves. This MEDT study elucidates the reaction mechanism of the considered reactions and emphasizes the importance of electron density analysis in understanding organic reactivity. Furthermore, molecular docking studies were performed to assess the potential of the DA products as antimicrobial agents against E. coli and S. aureus. Among the tested compounds, **P6-*endo*** showed the highest potential for efficacy against E. coli bacteria. However, **P1-*exo*** and **P6-*exo*** exhibited the most significant potential activity against S. aureus bacteria. The compounds generally show promising pharmacological properties with no significant toxicity effect.

Acknowledgements

This project has received funding from the European Union's Horizon 2020 research and innovation programme under the Marie Sklodowska-Curie grant agreement No 872081. A.G.-V. acknowledges funding by the Ministerio de Ciencia e Innovación (MICINN, Spain), Grant No. PID2021-122796NB-I00. The authors acknowledge the Moroccan Association of Theoretical Chemists for providing the computational programs.

References

1. Sadowski M., and Kula K. (**2024**) Nitro-functionalized analogues of 1,3-Butadiene: An overview of characteristic, synthesis, chemical transformations and biological activity. *Curr. Chem. Lett.,* 13, 15–30. https://doi.org/10.5267/j.ccl.2023.9.003
2. Jasiński R. (**2021**) On the Question of Stepwise [4+2] Cycloaddition Reactions and Their Stereochemical Aspects. *Symmetry*, 13, 1911. https://doi.org/10.3390/sym13101911
3. Carosso S., and Miller M. J. (**2014**) Nitroso Diels–Alder (NDA) reaction as an efficient tool for the functionalization of diene-containing natural products. *Org. Biomol. Chem*., 12, 7445–7468. https://doi.org/10.1039/C4OB01033G
4. Gregoritza M., and Brandl F. P. (**2015**) The Diels–Alder reaction: A powerful tool for the design of drug delivery systems and biomaterials. *Eur. J. Pharm. Biopharm*., 97, 438–453. https://doi.org/10.1016/j.ejpb.2015.06.007
5. Eschenbrenner-Lux V., Kumar K., and Waldmann H. (**2014**) The Asymmetric Hetero-Diels–Alder Reaction in the Syntheses of Biologically Relevant Compounds. *Angew. Chem. Int. Ed*., 53, 11146–11157. https://doi.org/10.1002/anie.201404094
6. Byun Y., and Coskun A. (**2018**) Epoxy-Functionalized Porous Organic Polymers via the Diels–Alder Cycloaddition Reaction for Atmospheric Water Capture. *Angew. Chem. Int. Ed*., 57, 3173–3177. https://doi.org/10.1002/anie.201800380
7. Andrew T. L., Cox J. R., and Swager T. M. (**2010**) Synthesis, Reactivity, and Electronic Properties of 6,6-Dicyanofulvenes. *Org. Lett*., 12, 5302–5305. https://doi.org/10.1021/ol102384k

8. Alameddine B., Baig N., Shetty S., et al (**2018**) Microwave-Assisted [4+2] Diels–Alder Cycloaddition of 1,4-Diethynyl Triptycene with Various Cyclopentadienone Derivatives: Promising Building Blocks for Polymer Networks. *Asian J. Org. Chem*., 7, 378–382. https://doi.org/10.1002/ajoc.201700655
9. Oppolzer W., Chapuis C., Dupuis D., and Guo M. (**1985**) Asymmetric *Diels - Alder* Reactions of Neopentyl-Ether-Shielded Acrylates and Allenic Esters: Syntheses of (−)-Norbornenone and (−)-β-Santalene. *Helv. Chim. Act*, 68, 2100–2114. https://doi.org/10.1002/hlca.19850680803
10. Kueh J. T. B., Stanley N.J., Hewitt R. J., et al (**2017**) Norborn-2-en-7-ones as physiologically-triggered carbon monoxide-releasing prodrugs. *Chem. Sci*., 8, 5454–5459. https://doi.org/10.1039/C7SC01647F
11. Payne C. M., Cho K., and Larsen D. S. (**2019**) 5-Bromo-norborn-2-en-7-one derivatives as a carbon monoxide source for palladium catalyzed carbonylation reactions. *RSC Adv*., 9, 30736–30740. https://doi.org/10.1039/C9RA06594F
12. Zhang Y-L., Zhou X-W., Wang X-B., et al (**2017**) Xylopiana A, a Dimeric Guaiane with a Case-Shaped Core from *Xylopia vielana* : Structural Elucidation and Biomimetic Conversion. *Org. Lett*., 19, 3013–3016. https://doi.org/10.1021/acs.orglett.7b01276
13. Qin J. J., Jin H. Z., Fu J. J., et al (**2009**) Japonicones A–D, bioactive dimeric sesquiterpenes from Inula japonica Thunb. *Bioorg. Med. Chem. Lett*., 19, 710–713. https://doi.org/10.1016/j.bmcl.2008.12.043
14. Li D., Liu G., Hu Q., et al (**2007**) Lewis Acid Promoted Tandem Intermolecular Diels−Alder/Intramolecular Allylation Reactions of Silyl-Substituted 1,3-Butadienes Leading to Multisubstituted 7-Norbornenones and Related Polycyclic Compounds*. Org. Lett*., 9, 5433–5436. https://doi.org/10.1021/ol702379s
15. Dong S., Hamel E., Bai R., et al (**2009**) Enantioselective Synthesis of (+)-Chamaecypanone C: A Novel Microtubule Inhibitor. *Angew. Chem*., 121, 1522–1525. https://doi.org/10.1002/ange.200805486
16. Fleming I., and Michael J.P. (**1981**) Synthetic studies with 7-functionalised norbornenes, and their synthesis by a silicon-controlled carbocation rearrangement. *J. Chem. Soc*., *Perkin Trans*, 1 1549. https://doi.org/10.1039/p19810001549
17. Liu S., Wang J., Ma Y., et al (**2022**) Construction of alkyl-substituted 7-norbornenones through Diels−Alder cycloaddition of electron-deficient olefins and a cyclopentadienone derivative generated in situ. *Chin. Chem. Lett*., 33, 2041–2043. https://doi.org/10.1016/j.cclet.2021.09.030
18. Domingo L. (**2016**) Molecular Electron Density Theory: A Modern View of Reactivity in Organic Chemistry. *Molecules*, 21, 1319. https://doi.org/10.3390/molecules21101319
19. Calais J. (**1993**) Density-functional theory of atoms and molecules. R.G. Parr and W. Yang, Oxford University Press, New York, Oxford, 1989. IX + 333 pp. Price £45.00. I*nt. J. Quantum Chem*., 47, 101–101. https://doi.org/10.1002/qua.560470107
20. Domingo L. R., Ríos-Gutiérrez M., and Aurell M. J. (**2021**) Unveiling the Ionic Diels–Alder Reactions within the Molecular Electron Density Theory. *Molecules*, 26, 3638. https://doi.org/10.3390/molecules26123638
21. Domingo L. R., Ríos-Gutiérrez M., and Pérez P. (**2018**) A Molecular Electron Density Theory Study of the Reactivity and Selectivities in [3 + 2] Cycloaddition Reactions of *C* , *N* -Dialkyl Nitrones with Ethylene Derivatives. *J. Org. Chem*., 83, 2182–2197. https://doi.org/10.1021/acs.joc.7b03093
22. Domingo L. R., Ríos-Gutiérrez M., and Aurell M. J. (**2021**) Unveiling the Intramolecular Ionic Diels–Alder Reactions within Molecular Electron Density Theory. *Chemistry*, 3, 834–853. https://doi.org/10.3390/chemistry3030061
23. Domingo L. R., Pérez P., Ríos-Gutiérrez M., and Aurell M. J. (**2024**) A molecular electron density theory study of hydrogen bond catalysed polar Diels–Alder reactions of α,β-unsaturated carbonyl compounds. *Tetrahedron Chem*., 10, 100064. https://doi.org/10.1016/j.tchem.2024.100064
24. Benhamed L., Mekelleche S. M., and Benchouk W. (**2021**) Theoretical Insight into the Reversal of Chemoselectivity in Diels-Alder Reactions of α,β-Unsaturated Aldehydes and Ketones Catalyzed by Brønsted and Lewis Acids. *Organics*, 2, 38–49. https://doi.org/10.3390/org2010004
25. Hallooman D., Cudian D., Ríos-Gutiérrez M., et al (**2017**) Understanding the Intramolecular Diels-Alder Reactions of N-Substituted N-Allyl-Furfurylamines: An MEDT Study. *ChemistrySelect*., 2, 9736–9743. https://doi.org/10.1002/slct.201702136
26. Domingo L. R., and Pérez P. (**2020**) Lithium Cation-Catalyzed Benzene Diels–Alder Reaction: Insights on the Molecular Mechanism Within the Molecular Electron Density Theory. *J. Org. Chem*., 85, 13121–13132. https://doi.org/10.1021/acs.joc.0c01801
27. Domingo L. R., Ríos-Gutiérrez M., and Pérez P. (**2020**) A molecular electron density theory study of the participation of tetrazines in aza-Diels–Alder reactions. *RSC Adv*., 10, 15394–15405. https://doi.org/10.1039/D0RA01548B
28. Kim C., Riley A., Sriharan S., et al (**2024**) Examining Antimicrobial Resistance in Escherichia coli: A Case Study in Central Virginia's Environment. *Antibiotics*, 13, 223. https://doi.org/10.3390/antibiotics13030223
29. Tong S. Y. C., Davis J. S., Eichenberger E., et al (**2015**) Staphylococcus aureus Infections: Epidemiology, Pathophysiology, Clinical Manifestations, and Management. *Clin. Microbiol. Rev*., 28, 603–661. https://doi.org/10.1128/CMR.00134-14
30. Lee C., Yang W., and Parr R. G. (**1988**) Development of the Colle-Salvetti correlation-energy formula into a functional of the electron density. *Phys. Rev. B*, 37, 785–789. https://doi.org/10.1103/PhysRevB.37.785
31. Becke A. D. (**1992**) Density-functional thermochemistry. I. The effect of the exchange-only gradient correction. *J. Chem. Phys*., 96, 2155–2160. https://doi.org/10.1063/1.462066

32. Schlegel H. B. (**1982**) Optimization of equilibrium geometries and transition structures. *J. Comput. Chem*., 3, 214–218. https://doi.org/10.1002/jcc.540030212
33. Gonzalez C., and Schlegel H. B. (**1989**) An improved algorithm for reaction path following. *J. Chem. Phys*., 90, 2154–2161. https://doi.org/10.1063/1.456010
34. Cossi M., Barone V., Cammi R., and Tomasi J. (**1996**) Ab initio study of solvated molecules: a new implementation of the polarizable continuum model. *Chem. Phys. Lett*., 255, 327–335. https://doi.org/10.1016/0009-2614(96)00349-1
35. Barone V., Cossi M., and Tomasi J. (**1998**) Geometry optimization of molecular structures in solution by the polarizable continuum model. *J. Comput. Chem*., 19, 404–417. https://doi.org/10.1002/(SICI)1096-987X(199803)19:4<404::AID-JCC3>3.0.CO;2-W
36. Geerlings P., De Proft F., and Langenaeker W. (**2003**) Conceptual Density Functional Theory. *Chem. Rev*., 103, 1793–1874. https://doi.org/10.1021/cr990029p
37. Domingo L., Ríos-Gutiérrez M., and Pérez P. (**2016**) Applications of the Conceptual Density Functional Theory Indices to Organic Chemistry Reactivity. *Molecules*, 21, 748. https://doi.org/10.3390/molecules21060748
38. Parr R. G., Szentpály L. V., and Liu S. (**1999**) Electrophilicity Index. *J. Am. Chem. Soc*., 121, 1922–1924. https://doi.org/10.1021/ja983494x
39. Pearson R. G. (**1992**) The electronic chemical potential and chemical hardness. *J. Mol. Struct. THEOCHEM*, 255, 261–270. https://doi.org/10.1016/0166-1280(92)85014-C
40. Domingo L. R., and Pérez P. (**2011**) The nucleophilicity N index in organic chemistry. *Org. Biomol. Chem*., 9, 7168. https://doi.org/10.1039/c1ob05856h
41. Domingo L. R., Pérez P., and Sáez J. A. (**2013**) Understanding the local reactivity in polar organic reactions through electrophilic and nucleophilic Parr functions. *RSC Adv*., 3, 1486–1494. https://doi.org/10.1039/C2RA22886F
42. Domingo L. R. (**2014**) A new C–C bond formation model based on the quantum chemical topology of electron density. *RSC Adv*., 4, 32415–32428. https://doi.org/10.1039/C4RA04280H
43. Reed A. E., Weinstock R. B., and Weinhold F. (**1985**) Natural population analysis. *J. Chem. Phys*., 83, 735–746. https://doi.org/10.1063/1.449486
44. Reed A. E., Curtiss L. A., and Weinhold F. (**1988**) Intermolecular interactions from a natural bond orbital, donor-acceptor viewpoint. *Chem. Rev*., 88, 899–926. https://doi.org/10.1021/cr00088a005
45. Frisch M. J., Trucks G. W., Schlegel H. B., Scuseria G. E., Robb M. A., Cheeseman J. R., Scalmani G., Barone V., Petersson G. A., Nakatsuji H., Li X., Caricato M., Marenich A. V., Bloino J., Janesko B. G., Gomperts R., Mennucci B., Hratchian H. P., Ortiz J. V., Izmaylov A. F., Sonnenberg J. L., Williams-Young D., Ding F., Lipparini F., Egidi F., Goings J., Peng B., Petrone A., Henderson T., Ranasinghe D., Zakrzewski V. G., Gao J., Rega N., Zheng G., Liang W., Hada M., Ehara M., Toyota K., Fukuda R., Hasegawa J., Ishida M., Nakajima T., Honda Y., Kitao O., Nakai H., Vreven T., Throssell K., Montgomery J. A. Jr., Peralta J. E., Ogliaro F., Bearpark M. J., Heyd J. J., Brothers E. N., Kudin K. N., Staroverov V. N., Keith T. A., Kobayashi R., Normand J., Raghavachari K., Rendell A. P., Burant J. C., Iyengar S. S., Tomasi J., Cossi M., Millam J. M., Klene M., Adamo C., Cammi R., Ochterski J. W., Martin R. L., Morokuma K., Farkas O., Foresman J. B., and Fox D. J. (**2016**) Gaussian 16, Revision B.01, Gaussian, Inc., Wallingford, CT.
46. Bader R. F. W., and Essén H. (**1984**) The characterization of atomic interactions. *J. Chem. Phys*., 80, 1943–1960. https://doi.org/10.1063/1.446956
47. Bader R. F. W, Anderson S. G, and Duke A. J (**1979**) Quantum topology of molecular charge distributions. 1. *J. Am. Chem. Soc*., 101, 1389–1395. https://doi.org/10.1021/ja00500a006
48. Bader R. F. W., Nguyen-Dang T. T., and Tal Y. (**1979**) Quantum topology of molecular charge distributions. II. Molecular structure and its change. *J. Chem. Phys*., 70, 4316–4329. https://doi.org/10.1063/1.438006
49. Lu T., and Chen Q. (**2022**) Independent gradient model based on Hirshfeld partition: A new method for visual study of interactions in chemical systems. *J. Comput. Chem*., 43, 539–555. https://doi.org/10.1002/jcc.26812
50. Lefebvre C., Khartabil H., Boisson J., et al (**2018**) The Independent Gradient Model: A New Approach for Probing Strong and Weak Interactions in Molecules from Wave Function Calculations. *ChemPhysChem*., 19, 724–735. https://doi.org/10.1002/cphc.201701325
51. Lu T., and Chen F. (**2012**) Multiwfn: A multifunctional wavefunction analyzer. *J. Comput. Chem*., 33, 580–592. https://doi.org/10.1002/jcc.22885
52. Becke A. D, and Edgecombe K. E (**1990**) A simple measure of electron localization in atomic and molecular systems. *J. Chem. Phys*., 92, 5397–5403. https://doi.org/10.1063/1.458517
53. Silvi B., and Savin A. (**1994**) Classification of chemical bonds based on topological analysis of electron localization functions. *Nature*, 371, 683–686. https://doi.org/10.1038/371683a0
54. Noury S., Krokidis X., Fuster F., and Silvi B. (**1999**) Computational tools for the electron localization function topological analysis. *Comput. Chem*., 23, 597–604. https://doi.org/10.1016/S0097-8485(99)00039-X
55. Dennington R., Keith T. A., and Millam J. M. (**2016**) GaussView, Version 6.1. Semichem Inc., Shawnee Mission, KS.
56. Humphrey W., Dalke A., and Schulten K. (**1996**) VMD: Visual molecular dynamics. *J. Mol. Graph*., 14, 33–38. https://doi.org/10.1016/0263-7855(96)00018-5
57. Trott O., and Olson A. J. (**2010**) AutoDock Vina: Improving the speed and accuracy of docking with a new scoring function, efficient optimization, and multithreading. *J. Comput. Chem*., 31, 455–461. https://doi.org/10.1002/jcc.21334

58. Vilar S., Cozza G., and Moro S. (**2008**) Medicinal Chemistry and the Molecular Operating Environment (MOE): Application of QSAR and Molecular Docking to Drug Discovery. *Cur*. *Top Med*. *Chem*., 8, 1555–1572. https://doi.org/10.2174/156802608786786624
59. Krokidis X., Noury S., and Silvi B. (**1997**) Characterization of Elementary Chemical Processes by Catastrophe Theory. *J*. *Phys*. *Chem*. *A*, 101, 7277–7282. https://doi.org/10.1021/jp9711508
60. Sadowski M., Dresler E., Wróblewska A., and Jasiński R. (**2024**) A New Insight into the Molecular Mechanism of the Reaction between 2-Methoxyfuran and Ethyl (Z)-3-phenyl-2-nitroprop-2-enoate: An Molecular Electron Density Theory (MEDT) Computational Study. *Molecules*, 29,4876. https://doi.org/10.3390/molecules29204876
61. Sadowski M., Synkiewicz-Musialska B., and Kula K. (**2024**) (1E,3E)-1,4-Dinitro-1,3-butadiene—Synthesis, Spectral Characteristics and Computational Study Based on MEDT, ADME and PASS Simulation. *Molecules*, 29, 542. https://doi.org/10.3390/molecules29020542
62. Dresler E., Wróblewska A., and Jasiński R. (**2023**) Understanding the Molecular Mechanism of Thermal and LA-Catalysed Diels–Alder Reactions between Cyclopentadiene and Isopropyl 3-Nitroprop-2-Enate. *Molecules*, 28, 5289. https://doi.org/10.3390/molecules28145289
63. Woliński P., Kącka-Zych A., Wróblewska A., et al (**2023**) Fully Selective Synthesis of Spirocyclic-1,2-oxazine N-Oxides via Non-Catalysed Hetero Diels-Alder Reactions with the Participation of Cyanofunctionalysed Conjugated Nitroalkenes. *Molecules*, 28, 4586. https://doi.org/10.3390/molecules28124586
64. Rafik A., El Hadki H., Jaddi A., et al (**2024**) A new investigation into the regioselectivity and stereoselectivity of the reaction between di-methyl nitrone and fluorinated alkenes: DFT, independent gradient model, and molecular docking. *Comput*. *Theor*. *Chem*., 1234, 114511. https://doi.org/10.1016/j.comptc.2024.114511
65. Domingo L.R., and Ríos-Gutiérrez M. (**2023**) A Useful Classification of Organic Reactions Based on the Flux of the Electron Density. *Sci*. *Rad*., 2, 1–24. https://doi.org/10.58332/scirad2023v2i1a01
66. Ríos-Gutiérrez M., Saz Sousa A., and Domingo L. R. (**2023**) Electrophilicity and nucleophilicity scales at different DFT computational levels. *J*. *Phys*. *Org*. *Chem*., 36, e4503. https://doi.org/10.1002/poc.4503
67. Jasiński R. (**2015**) A stepwise, zwitterionic mechanism for the 1,3-dipolar cycloaddition between (Z)-C-4-methoxyphenyl-N-phenylnitrone and gem-chloronitroethene catalysed by 1-butyl-3-methylimidazolium ionic liquid cations. *Tetrahedron Lett*., 56, 532–535. https://doi.org/10.1016/j.tetlet.2014.12.007
68. Domingo L. R., and Sáez J. A. (**2011**) Understanding the Electronic Reorganization along the Nonpolar [3 + 2] Cycloaddition Reactions of Carbonyl Ylides. *J*. *Org*. *Chem*., 76, 373–379. https://doi.org/10.1021/jo101367v
69. Weiss R., Cornaton Y., Khartabil H., et al (**2022**) Deciphering the Role of Noncovalent Interactions in the Conformations of Dibenzo-1,5-dichalcogenocines. *ChemPlusChem*., 87:e202100518. https://doi.org/10.1002/cplu.202100518
70. Rafik A., Jaddi A., Salah M., et al (**2024**) Insights into the mechanism, selectivity, and substituent effects in the Diels-Alder reaction of azatrienes with electron-rich dienophiles: An MEDT study. *J*. *Mol*. *Graph*. *Model*., 132, 108819. https://doi.org/10.1016/j.jmgm.2024.108819
71. Roby O., Kadiri F. Z., Loukhmi Z., et al (**2023**) Synthesis of new set of imidazo[1,2-a]pyridine-schiff bases derivatives as potential antimicrobial agents: Experimental and theoretical approaches. *J*. *Mol*. *Struct*., 1292, 136186. https://doi.org/10.1016/j.molstruc.2023.136186